

Multi-scale Interaction for Real-time LiDAR Data Segmentation on an Embedded Platform

Shijie Li, Xieyuanli Chen, Yun Liu, Dengxin Dai, Cyrill Stachniss, Juergen Gall

Abstract—Real-time semantic segmentation of LiDAR data is crucial for autonomously driving vehicles, which are usually equipped with an embedded platform and have limited computational resources. Approaches that operate directly on the point cloud use complex spatial aggregation operations, which are very expensive and difficult to optimize for embedded platforms. They are therefore not suitable for real-time applications with embedded systems. As an alternative, projection-based methods are more efficient and can run on embedded platforms. However, the current state-of-the-art projection-based methods do not achieve the same accuracy as point-based methods and use millions of parameters. In this paper, we therefore propose a projection-based method, called Multi-scale Interaction Network (MINet), which is very efficient and accurate. The network uses multiple paths with different scales and balances the computational resources between the scales. Additional dense interactions between the scales avoid redundant computations and make the network highly efficient. The proposed network outperforms point-based, image-based, and projection-based methods in terms of accuracy, number of parameters, and runtime. Moreover, the network processes more than 24 scans per second on an embedded platform, which is higher than the framerates of LiDAR sensors. The network is therefore suitable for autonomous vehicles.

Index Terms—Real-time semantic segmentation, autonomous driving, LiDAR sensor, embedded platform.



1 INTRODUCTION

Environment perception and understanding are key to realize self-driving cars. For the full-view perception of the environment, autonomously driving vehicles are usually equipped with multi-sensor systems, among which light detection and ranging (LiDAR) sensors play a key role due to their precise distance measurements. The large point clouds that are generated by the LiDAR sensors, however, need to be interpreted in order to understand the environment.

Although Convolution Neural Networks (CNNs) perform well for semantic image segmentation [1], [2], [3], [4], [5], [6], [7], they cannot be applied directly to 3D point clouds. This is because standard convolutions require a regular grid structure, whereas a raw point cloud is an unordered structure. To address this problem, some methods [8], [9], [10], [11] try to directly process point clouds using some spatial aggregation operations like grouping and gathering. Although these methods work well in indoor scenarios, it is difficult to apply them to large outdoor scenarios. In particular the computational cost of the aggregation operation increases with the number of points, making these methods too inefficient for autonomous driving. Another issue is that it is hard to optimize point-based methods for better efficiency using modern technology like TensorRT due to many complex operations, preventing them from being easily deployed on an embedded platform. However, runtime efficiency is of vital importance for real-world applications, especially for autonomously driving vehicles. Therefore, point-based methods are not directly applicable to autonomous driving.

Wu *et al.* [12], [13] found that point clouds produced by a LiDAR sensor can be represented as an ordered projected image, so CNNs can then be applied. However, projected LiDAR data and RGB images are different modalities and applying directly 2D image-based methods does not result in a good performance. For this reason, some specific CNNs have been designed for LiDAR-based range images, named as projection-based methods. The current state-of-the-art projection-based method [14], however, is very large with more than 50M parameters, making it inefficient for embedded platforms.

In this work, we therefore propose a novel projection-based method that achieves a high accuracy, but runs at a higher frame rate on an embedded platform than a LiDAR sensor. This is achieved by three contributions. First, we propose a very efficient multi-scale architecture, which balances the computational resources across the different scales in an optimal way. We therefore term the network Multi-scale Interaction Network (MINet). Second, we provide additional supervision, which improves the accuracy without increasing the runtime or memory consumption for inference. Third, we first process the different modalities independently before fusing them, which also increases the accuracy. We explain the three contributions more in detail.

Dealing with large scale variations of objects in outdoor scenes is an important challenge for autonomous driving. While this can be addressed by multi-scale approaches, they come at high computational cost. In this work, we therefore propose an efficient multi-path architecture as shown in Fig. 1 where each path operates on different scales and the paths interact with each other. We use three paths with decreasing resolution and increasing receptive field from top to bottom. In contrast to standard multi-scale approaches, that use the same operations for each resolution, we adapt the computational operations for each path. While

-
- S. Li, X. Chen, C. Stachniss, and J. Gall are with Bonn University, German, 53115. J. Gall (gall@iai.uni-bonn.de) is the corresponding author.
 - Y. Liu is with College of Computer Science, Nankai University, China.
 - D. Dai is with ETH Zurich, Switzerland.

Manuscript received April 19, 2005; revised August 26, 2015.

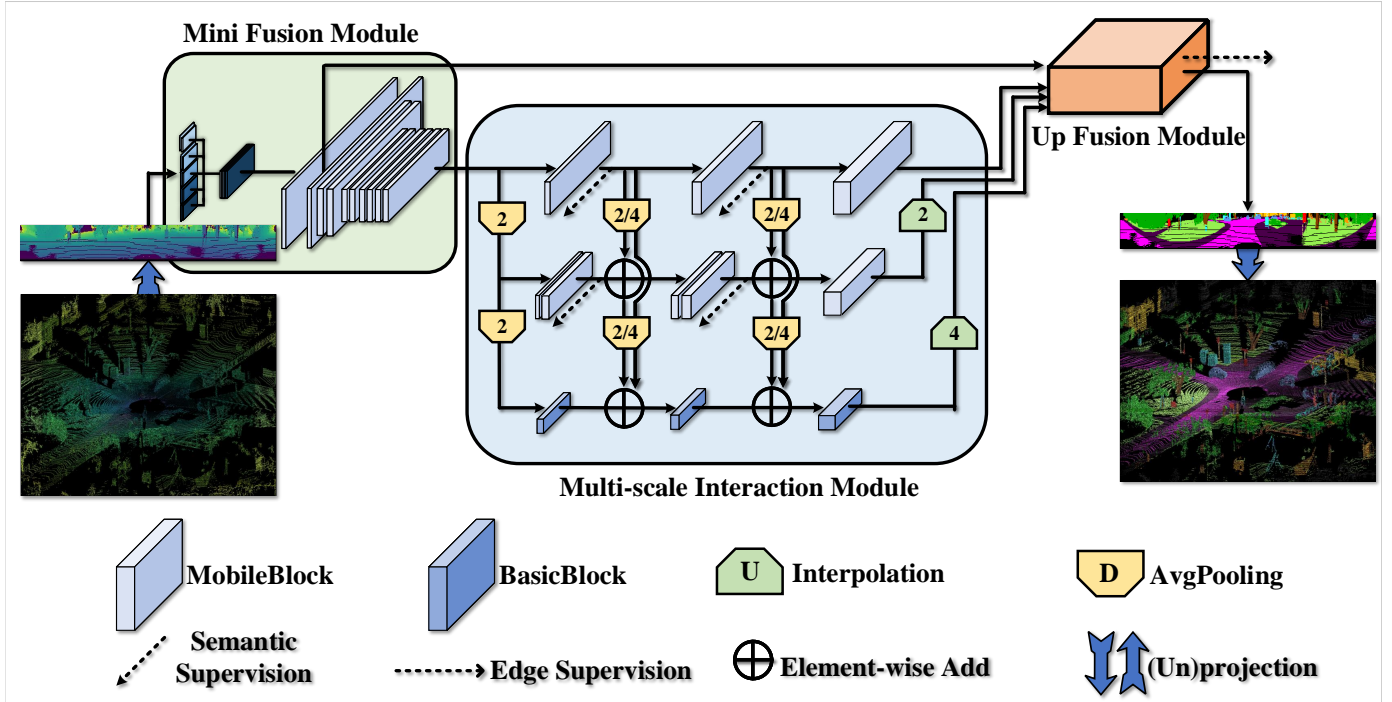


Fig. 1: Illustration of the Multi-scale Interaction Network architecture. The numbers 2 and 4 for interpolation (U) and average pooling (D) indicate the upsampling and downsampling factor. The dashed arrows indicate the supervision type.

the top path extracts low-level clues, which can be easily detected with shallow layers operating on high-resolution feature maps, the bottom path extracts high-level semantic information which requires more complex operations, but on low-resolution feature maps. In order to avoid redundant computations across the paths, we propose a dense top-to-bottom interaction strategy where feature maps from a path are passed to all lower paths. Hence, this design achieves a good balance between effectiveness and efficiency.

As it has been shown in some recent works [2], [15], [16], [17], adding additional supervision can improve the accuracy. In contrast to these works, however, we propose to add different types of supervision at different parts of the network, which is more effective. Finally, we process the multi-modal data consisting of 3D coordinates, remission, and range information first independently and then fuse them in the feature space. This is in contrast to previous works that just concatenate the modalities and therefore ignore that the characteristics of each modality is different.

In summary, our contributions include:

- We propose a multi-scale approach where the computational operations are balanced across the different scales and a top-to-bottom interaction strategy avoids redundant computations.
- We exploit different types of additional supervision to improve the accuracy without increasing the inference time.
- Different from previous methods, we process each modality independently and fuse them in the feature space, which improves the overall segmentation performance.
- By incorporating the above design decisions, we propose a lightweight projection-based model for semantic segmentation of LiDAR data that runs in

real-time on an embedded platform.

The experimental results demonstrate that our method reduces the number of parameters by about 98% and is about $4\times$ faster than the state-of-the-art projection-based method [14], while achieving a higher accuracy. We also evaluate our model on an embedded platform and demonstrate that our method can be deployed for autonomous driving. The code will be released in case of acceptance.

2 RELATED WORK

2.1 Image-based Semantic Segmentation

We first briefly review some 2D semantic segmentation methods for RGB images. FCN [1] and U-Net [18] introduce fully convolutional networks to make pixel-wise predictions. The first version of DeepLab [19] proposed dilated convolutions to enlarge the receptive field, and a conditional random field (CRF) is applied as post-processing to refine the segmentation results. The later variants of DeepLab [20], [21], [22] adopt dilated convolutions with different dilation rates for multi-scale feature learning. PSPNet [2] designs a pyramid pooling module to extract global contextual information. Recent progress for 2D segmentation comes with the success of attention mechanisms. DANet [23] applies spatial attention and channel-wise attention at the top of networks to enhance feature learning. CCNet [3] and ANN [4] present simplified and efficient versions of the non-local attention module [24] and adapt it to semantic segmentation. Apart from these methods, some methods focus on the efficiency. MobileNets [25], [26], [27] utilize depthwise convolutions to reduce the model size with little performance degradation. Different from MobileNets, ShuffleNets [28], [29] achieve the same goal by channel shuffle. However, these image-based methods are designed for 2D

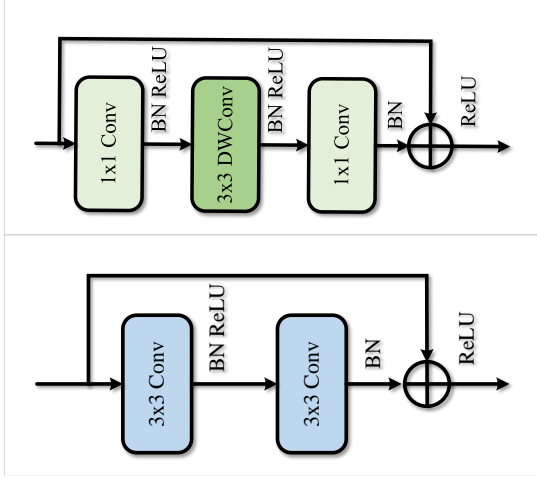


Fig. 2: Illustration of the MobileBlock (top) and the BasicBlock (bottom). DWConv means depth-wise convolution.

RGB images and cannot process 3D points like LiDAR data directly. Since even applying them on projected LiDAR data does not result in a very good performance due to the different modalities, specific projection-based methods have been proposed for LiDAR data as we will discuss in Sec. 2.3.

2.2 Point-based Semantic Segmentation

Although CNNs are successful for 2D image-based semantic segmentation, they cannot handle unstructured data like point clouds. To address this problem, tangent convolutions [30] project local points to a tangent plane and vanilla convolutions are then applied to it. PointNet [8] is the first method that directly processes the point cloud. It applies a convolution operation for each point and uses a permutation invariant operation to aggregate information. However, PointNet does not take local information into consideration, which is realized by PointNet++ [9]. Apart from these methods, some works focus on defining new convolution operations for point clouds such as PointConv [11] and KP-FCNN [31]. SPGraph [32] tackles semantic segmentation of large-scale point clouds by defining a super point graph (SPG). Because point-based methods are inefficient for large point clouds, RandLA [33] addresses this problem by adopting random sampling and designing a better grouping strategy to maintain a better performance. P²Net [34] applies point-based methods on projected LiDAR data. However, these methods are too expensive for many applications, especially for embedded platforms.

2.3 Projection-based Semantic Segmentation

Projection-based segmentation methods project LiDAR point clouds onto 2D multi-modal images and use 2D CNNs for semantic segmentation. SqueezeSeg [12] and SqueezeSegV2 [13] use a lightweight network called SqueezeNet [35] for semantic segmentation and a CRF for post-processing. Based on SqueezeSeg, RangeNet++ [14] adopts Darknet [36] and replaces the CRF with a k -NN for post-processing. It has also been successfully used to improve LiDAR-based odometry [37] and loop closure detection [38]. Current projection-based methods, however, do not achieve the same segmentation accuracy as point-based methods and

Module	Operation	k	c	s	t	Output size
MFM	Conv2d	3	4	1	5	64×2048
	MobileBlock	3	20	1	1	64×2048
	MobileBlock	3	24	2	1	32×512
	MobileBlock	3	24	1	1	32×512
	MobileBlock	5	40	2	1	16×256
	MobileBlock	5	40	1	1	16×256
	MobileBlock	5	40	1	1	16×256
	MobileBlock	3	80	1	1	16×256
	MobileBlock	3	80	1	1	16×256
	MobileBlock	3	80	1	1	16×256
	MobileBlock	3	80	1	1	16×256
	Conv2d	1	32	0	1	16×256
MIM	MobileBlock	3	64	1	1	16×256
	MobileBlock	3	128	1	1	16×256
	MobileBlock	3	128	1	1	16×256
	MobileBlock	3	32	1	1	8×128
	MobileBlock	3	64	1	1	8×128
	MobileBlock	3	64	1	1	8×128
	MobileBlock	3	128	1	1	8×128
	MobileBlock	3	128	1	1	8×128
	BasicBlock	3	64	1	1	4×64
UFM	Conv2d	3	32	1	1	16×512
	Conv2d	3	32	1	1	64×2048
	Conv2d	1	32	1	1	64×2048
	BasicBlock	3	128	1	1	4×64
	BasicBlock	3	128	1	1	4×64
	BasicBlock	3	128	1	1	4×64

TABLE 1: Instantiation of the Multi-scale Interaction Network. Each module contains several components: Conv2d, MobileBlock, and BasicBlock. While Conv2d denotes a convolutional layer followed by one batch normalization layer and ReLU activation, MobileBlock and BasicBlock are illustrated in Fig. 2. Each operation has a kernel size k , stride s , and output channels c , repeated t times. The three sections of the Multi-scale Interaction Module (MIM) denote the three paths.

the best performing approaches use very large networks. In this paper, we propose a novel lightweight model that can run in real-time on an embedded platform while achieving state-of-the-art performance.

3 MULTI-SCALE INTERACTION NETWORK

Our Multi-scale Interaction Network (MINet) operates on projected images generated from LiDAR point clouds. To associate a LiDAR point to a pixel in the projected image, the transformation is formulated as:

$$u = \frac{1}{2}[1 - \arctan(y, x)\pi^{-1}]w, \quad (1)$$

$$v = [1 - (\arcsin(zr^{-1}) + o_{up})o^{-1}]h. \quad (2)$$

Here, we associate a LiDAR point $\mathbf{a}_i = (x, y, z)$ to a pixel (u, v) in the projected image of size (h, w) . The vertical field-of-view of the LiDAR is $o = o_{up} + o_{down}$ and $r = \|\mathbf{a}_i\|$ denotes the range of point i . After this transformation, a projected image with size $(h, w, 5)$ is generated, where each pixel includes coordinates (x, y, z) , range, and remission information of related 3D points.

The architecture of MINet is shown in Fig. 1. The projected image is first processed by the Mini Fusion Module (MFM) (Sec. 3.1) to fuse the multi-modal information in the feature space. In the Multi-scale Interaction Module (MIM) (Sec. 3.2), the data is processed at three different scales where the resolution is reduced by factor two for each path. As it is shown in Tab. 1, the computation differs for each path where we use two basic components,

namely MobileBlock and BasicBlock. The MobileBlock [25], [26] utilizes depthwise convolutions and has thus fewer parameters, but its learning capacity is also limited. The BasicBlock [39] is stronger, but also more expensive. MobileBlock and BasicBlock are shown in Fig. 2. We therefore balance the computational resources across the three paths as it is shown in Tab. 1. While we use the expensive BasicBlock for the bottom path with lowest resolution, we decrease the computational cost as the resolution increases using 5 MobileBlocks for the middle path and 3 for the top path. The connections from each path to lower paths avoid redundant computations at lower paths and make the network more efficient. Finally, the 2D predictions for the original resolution are produced by the Up Fusion Module (UFM) (Sec. 3.3), which are then mapped back to the 3D space. In the remainder of this section, we describe each module of the Multi-scale Interaction Network.

3.1 Mini Fusion Module

Different from an RGB image, the projected image contains channels of different modalities. Previous projection-based segmentation methods [12], [13], [14] treat such different modalities equally, but we show that processing each channel first independently is more efficient. Specifically, each channel of the multi-modal image is mapped to an independent feature space using 5 convolution blocks, including normalization and activation. This corresponds to the first row of Tab. 1. This step can be considered as a feature calibration step for each modality before fusing them. It needs to be noted that we also treat the x , y , and z coordinates separately. Combining them, however, did not improve the accuracy and requires to hardcode the input channels in the network architecture. Since this is not very desirable from a practical point of view, we process each channel at the beginning independently. After the first 5 convolutional layers, these features are concatenated and fed into several MobileBlocks for fusing them. Since a small resolution leads to less computation, the information of the feature maps are aggregated by average pooling gradually.

3.2 Multi-scale Interaction Module

After the fusion module, the data is processed by three paths where each path corresponds to a different scale as shown in Fig. 1. From top to bottom, the resolution of the feature maps is decreased by factor two using average pooling and the receptive field is accordingly increased. For the top path, we use the highest resolution. Since processing high resolution feature maps is very expensive, we use only three MobileBlocks as shown in Tab. 1. The bottom path, which has the largest receptive field and lowest resolution, can offer more abstract semantic clues if we use more expensive operations. Hence, it uses three BasicBlocks. The middle path is a compromise between the top and bottom path and consists of five MobileBlocks. In our experiments, we show that increasing the computational operations as the resolution decreases leads to a higher efficiency compared to using the same blocks for all paths. While the number of parameters doubles compared to the proposed architecture if we use the BasicBlocks for all paths, the accuracy drops if only MobileBlocks are used.

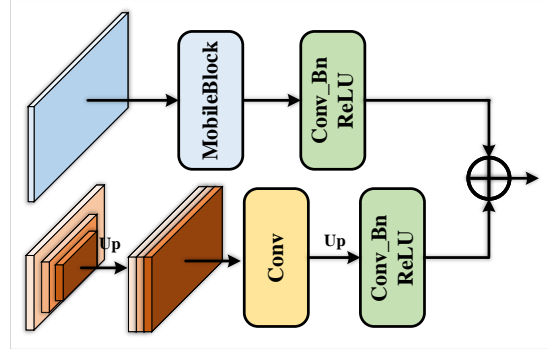


Fig. 3: Illustration of the Up Fusion Module.

A second important design choice of the Multi-scale Interaction Module is to allow interactions between the paths. Since the computational complexity of the paths increases for lower paths, we use a dense top-to-bottom fusion design for efficient multi-scale feature interaction. Especially, feature maps of the first and second path will be resized by average pooling and passed to all lower paths. To avoid a mismatch of the number of channels, the number of channels is increased gradually for each path and kept the same at each interaction position. Hence, no other operations are used to adjust the number of channels as shown in Tab. 1. Due to the interaction, the lower paths benefit from the features computed from higher paths. The lower paths can therefore focus on information that has not been extracted by higher paths due to limited computational resources.

3.3 Up Fusion Module

To obtain the semantic labels for each pixel of the projected input image, the Up Fusion Module shown in Fig. 3 combines the features from different scales and samples them up to the input resolution. In addition, features after the first MobileBlock of the Mini Fusion Module are used to recover detailed spatial information as shown in Fig. 1. The lower part of Fig. 3 shows the feature maps of the three different paths that are first resized to the same size, concatenated together, and fused by a 1×1 convolution. The fused feature maps are then upsampled to the original resolution and processed by a convolution block including a 3×3 convolution, batch normalization, and ReLU activation. The upper part shows the feature maps from the Mini Fusion Module that have already the original resolution. They are processed by a MobileBlock and a convolution block. Finally, the processed features from both modules are added together. Although the spatial information of the original feature maps already helps to sharpen segment boundaries, which can be fuzzy due to the upsampling, adding additional supervision for the segment boundaries emphasizes this effect as we will explain in the next section.

3.4 Booster Training Strategy

Adding supervision to intermediate parts of a network [40] has been shown to be useful for network optimization [2], [15], [16], [17]. In this work, we also use intermediate supervision, however, we propose two different types of supervision. Similar to balancing the computational resources

No.	MFM	Interaction	UFM	mIoU
1		✓	✓	50.9
2	✓		✓	50.7
3	✓	✓		50.6
4	✓	✓	✓	51.8

TABLE 2: Impact of the three modules.

across scales, it is very important to use the right supervision for the right part of the network.

We use the standard weighted cross-entropy loss as semantic supervision

$$\mathcal{L}_s = -\frac{1}{|I|} \sum_{i \in I} \sum_{n=1}^N w_n p_i^n \log(\hat{p}_i^n), \quad (3)$$

where N is the number of classes, p_i^n is the ground-truth semantic label for pixel i and class n ($p_i^n \in \{0, 1\}$), and \hat{p}_i^n is the predicted class probability. The weight w_n for class n is computed as in [14]. Besides at the end of the network, we use the weighted cross-entropy loss \mathcal{L}_s for the top and middle path as indicated by the dashed arrows in Fig. 1. As we will show in the experiments, this intermediate supervision improves the training and boosts the accuracy. Adding this semantic supervision to the bottom path, however, does not help since the resolution of the lower path is too low and downsampling of the ground-truth introduces too many artifacts.

As discussed in Sec. 3.3, obtaining accurate segment boundaries after upsampling is an issue. Since using CRFs for post-processing is very expensive and post-processing using k -NN performs even better for LiDAR data [14], we use additional supervision to guide the upsampling process. Inspired by [41], [42], we extract the semantic boundaries from the ground-truth labels and compare it to the semantic boundaries after upsampling. The semantic edge loss is then obtained by

$$\mathcal{L}_e = -\frac{1}{|I|} \sum_{i \in I} (e_i \log(\hat{e}_i) + (1 - e_i) \log(1 - \hat{e}_i)), \quad (4)$$

where e_i is the ground-truth edge label at pixel i ($e_i \in \{0, 1\}$) and \hat{e}_i is the predicted edge probability at pixel i .

Besides of the weighted cross entropy loss, which we denote by \mathcal{L}_{fs} and is computed in the same way as \mathcal{L}_s , we use the Lovász-Softmax loss \mathcal{L}_{ls} [43] at the end of the network, which maximizes the intersection-over-union (IoU) score:

$$\mathcal{L}_{ls} = \frac{1}{N} \sum_{n=1}^N \overline{\Delta_{J_n}}(m(n)), \quad (5)$$

$$m_i(n) = \begin{cases} 1 - \hat{p}_i^n & \text{if } n = p_i^n \\ \hat{p}_i^n & \text{otherwise,} \end{cases} \quad (6)$$

where $\overline{\Delta_{J_n}}$ defines the Lovász extension of the Jaccard index, $\hat{p}_i^n \in [0, 1]$ and $p_i^n \in \{0, 1\}$ denote for class n at pixel i the predicted probability and ground-truth label, respectively. In summary, the combined loss is given by

$$\mathcal{L} = \mathcal{L}_{fs} + \mathcal{L}_{ls} + \mathcal{L}_e + \lambda \sum_s \mathcal{L}_s \quad (7)$$

where λ is a weight and \mathcal{L}_s are the losses for the top and middle path. In our experiments, we empirically set λ to 0.1.

4 EXPERIMENTS

4.1 Experimental Settings

We use two challenging datasets to evaluate our method, namely SemanticKITTI [44] and SemanticPOSS [45]. Based on the KITTI Odometry Benchmark [46], SemanticKITTI provides a semantic label for each point in all scans. It includes over 43,000 scans from 21 sequences, among which sequences 00 to 10, which comprise over 21,000 scans, are available for training, and the remaining scans from sequences 11 to 21 are used for testing. Sequence 08 is used as validation set for hyperparameter selection and we train our approach on the remaining training set. SemanticPOSS is a smaller dataset with 2988 LiDAR scans that were captured at the Peking University. The point clouds of SemanticPOSS are more sparse compared to SemanticKITTI due to the lower resolution of the LiDAR sensor. Since the two datasets differ in size, LiDAR sensor, and environment, they provide an ideal testbed for evaluating the proposed approach.

4.1.1 Evaluation Metric

As for the evaluation metric, we calculate the standard mean intersection over union (mIoU) [47] over all classes:

$$\text{mIoU} = \frac{1}{N} \sum_{n=1}^N \frac{\text{TP}_n}{\text{TP}_n + \text{FP}_n + \text{FN}_n} \quad (8)$$

where TP_n , FP_n , and FN_n denote the numbers of true positive, false positive, and false negative predictions for class n , respectively. N is the number of classes.

4.1.2 Implementation details

All experiments are conducted on the same hardware with a single Quadro P6000. The selection of hyperparameters and ablation study are evaluated on the validation set (sequence 08) of the SemanticKITTI dataset. For the training, we use a learning rate of 0.003 and a decay of 0.99 in every epoch.

4.2 Ablation Study

4.2.1 Modules

As illustrated in Fig. 1, our network consists of three modules. In Tab. 2 we evaluate some design choices for the Mini Fusion Module (MFM) (Sec. 3.1), the Multi-scale Interaction Module (Interaction) (Sec. 3.2), and the Up Fusion Module (UFM) (Sec. 3.3). While the proposed approach achieves 51.8% mIoU (Row 4), we evaluate the impact of processing each modality separately before fusing them in the features space in the first row. To keep the number of parameters the same, we use 3×3 convolutions to process the input multi-modal image instead of processing each modality separately in the Mini Fusion Module. In this case, the accuracy drops by 0.9% (Row 1). This shows the benefit of processing each modality separately at the beginning. In Fig. 1, we have connections between the three paths. If we remove the top-to-down interactions, the accuracy is reduced by 1.1% (Row 2). This demonstrates the benefit of allowing interactions between the multi-scale features. If the multi-resolution features are just resized, concatenated, and processed by convolutional layers instead of using the proposed Up Fusion Module, the accuracy is reduced by 1.2% (Row 3).

No.	MIM			UFM	mIoU
	Top	Middle	Bottom		
1	S	S		E	51.8
2		S		E	50.3
3	S			E	50.2
4	S	S			50.5
5				E	49.0
6					48.4
7	S	S	S	E	50.9
8	S	S		S	50.8

TABLE 3: Impact of adding additional supervision. “S” denotes semantic supervision and “E” denotes edge supervision.

λ	0	0.01	0.1	1.0
mIoU	49.0	49.3	51.8	51.4

TABLE 4: Impact of λ in Equ. (7).

4.2.2 Supervision Setting

As discussed in Sec. 3.4, we use additional supervision for the Multi-scale Interaction Module (MIM) and the Up Fusion Module (UFM). For MIM, we use the semantic labels (S) to add a loss Equ. (3) to the top and middle path. For UFM, we add a loss Equ. (4) for the segment boundaries (E). In Tab. 3, we report the mIoU for different settings. The best setting is achieved by adding semantic supervision to the top and middle path in the Multi-scale Interaction Module and applying edge supervision to the Up Fusion Module (Row 1). Removing any of this additional supervision leads to an accuracy loss by more than 1.0% (Row 2-4). If the additional supervision is only used for the the Up Fusion Module, the accuracy even decreases further (Row 5). If we do not use any additional supervision, the accuracy is lowest and 3.4% below the proposed setting (Row 6). While we removed so far additional supervision, the last two rows in the table show results when we add or change the type of supervision. If we add additional supervision to the bottom path, the accuracy decreases by 0.9%. This is due to the large difference between the ground-truth resolution and the resolution of the bottom path, which results in sampling artifacts that have a negative impact. Instead of using the edge loss Equ. (4) for UFM, we also replaced it by the semantic loss that is used for MIM. While adding the semantic loss (Row 8) is better than using no additional loss for UFM (Row 4), the edge loss (Row 1) achieves a 1% higher accuracy than the semantic loss. This is expected since the purpose of the edge loss is to improve the segment boundaries after the upscaling, which is done by the Up Fusion Module.

4.2.3 Impact of λ

Our loss function Equ. (7) contains only one hyperparameter, namely λ . We evaluate the impact of λ in Tab. 4. The setting $\lambda = 0$ corresponds to row 5 of Tab. 3 where no additional supervision is added to the paths. We can see that $\lambda = 0.1$ achieves the best performance.

4.2.4 Path Settings

As shown in Tab. 1, we balance the computational resources across the three paths where we increase the complexity as the resolution decreases. In Tab. 5, we report the results

No.	Top	Middle	Bottom	Params(M)	GFLOP	SPS	mIoU
1	3×MB	5×MB	3×BB	1	6.2	59	51.8
2	3×MB	3×MB	3×MB	0.599	6.0	61	49.7
3	5×MB	5×MB	5×MB	0.628	6.3	58	50.2
4	3×BB	3×BB	3×BB	1.97	11.04	33	51.2

TABLE 5: Ablation study for the different blocks of each path. “MB” denotes MobileBlock, “BB” denotes BasicBlock, and “SPS” denotes scans per second.

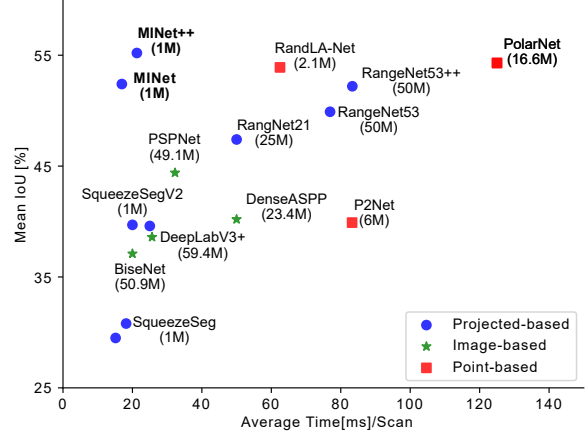


Fig. 4: Visualization of Tab. 6. We omit point-based methods that need more than 140ms per scan. The proposed Multi-scale Interaction Network (MINet) is not only the most accurate method, it also achieves the by far best trade-off between accuracy and runtime. ++ denotes k NN post-processing.

when we use the same operations for all paths, *i.e.*, either 3 or 5 MobileBlocks or 3 BasicBlocks. Using only MobileBlocks reduces the number of parameters, but it improves the runtime only slightly and this is only the case for 3 BasicBlocks. This, however, comes at a substantially lower accuracy. In terms of runtime and accuracy, the proposed setting provides a much better trade-off between runtime and accuracy. If the computationally expensive BasicBlocks are used for all paths, the number of parameters and runtime nearly doubles while the accuracy is nearly the same. This shows that using the same operations for all resolutions is highly inefficient and that the proposed approach achieves a good balance between efficiency and effectiveness.

4.3 Comparison with State-of-the-art Methods

We first compare the proposed Multi-scale Interaction Network (MINet) with other state-of-the-art methods on the SemanticKITTI test split in terms of both accuracy and efficiency. The results are shown in Tab. 6. In the first rows, we show the results for point-based methods. Most of the approaches are very slow and cannot process more than 2 scans per second since spatial aggregation operations are usually very time-consuming for large point clouds. The very recent works [33], [34], [49] are faster and process up to 16 scans per second, but it is difficult to optimize these networks for embedded systems due to their complex operations. The highest accuracy is achieved by [49], but the network is very large with over 16M parameters. Our proposed approach outperforms all point-based methods in terms of runtime, number of parameters, and accuracy.

	car	bicycle	motorcycle	truck	other-vehicle	person	bicyclist	motorcyclist	road	parking	sidewalk	other-ground	building	fence	vegetation	trunk	terrain	pole	traffic-sign	SPS	Params(M)	mIoU
Pointnet [8]	46.3	1.3	0.3	0.1	0.8	0.2	0.2	0.0	61.6	15.8	35.7	1.4	41.4	12.9	31.0	4.6	17.6	2.4	3.7	2	3	14.6
Pointnet++ [9]	53.7	1.9	0.2	0.9	0.2	0.9	1.0	0.0	72.0	18.7	41.8	5.6	62.3	16.9	46.5	13.8	30.0	6.0	8.9	0.1	6	20.1
SPGraph [32]	68.3	0.9	4.5	0.9	0.8	1.0	6.0	0.0	49.5	1.7	24.2	0.3	68.2	22.5	59.2	27.2	17.0	18.3	10.5	0.2	0.25	20.0
SPLATNet [48]	66.6	0.0	0.0	0.0	0.0	0.0	0.0	0.0	70.4	0.8	41.5	0.0	68.7	27.8	72.3	35.9	35.8	13.8	0.0	1	0.8	22.8
TangentConv [30]	86.8	1.3	12.7	11.6	10.2	17.1	20.2	0.5	82.9	15.2	61.7	9.0	82.8	44.2	75.5	42.5	55.5	30.2	22.2	0.3	0.4	35.9
P ² Net [34]	85.6	20.4	14.4	14.4	11.5	16.9	24.9	5.9	87.8	47.5	67.3	7.3	77.9	43.4	72.5	36.5	60.8	22.8	38.2	12.1	6	39.8
RandLA-Net [33]	94.2	26.0	25.8	40.1	38.9	49.2	48.2	7.2	90.7	60.3	73.7	20.4	86.9	56.3	81.4	61.3	66.8	49.2	47.7	16	2.1	53.9
PolarNet [49]	93.8	40.3	30.1	22.9	28.5	43.2	40.2	5.6	90.8	61.7	74.4	21.7	90.0	61.3	84.0	65.5	67.8	51.8	57.5	8	16.6	54.3
DeepLabV3+ [22]	78.4	13.6	9.5	9.5	10.4	17.5	22.0	0.4	88.5	54.5	66.7	9.7	77.9	39.1	72.0	39.9	60.0	23.4	36.1	39	59.4	38.4
PSPNet [50]	79.6	25.0	26.4	17.5	24.0	34.1	28.4	7.3	90.2	58.2	70.2	19.9	79.7	43.5	74.2	43.2	61.2	23.1	37.5	31	49.08	44.4
BiSeNet [51]	76.0	13.4	11.9	18.3	7.6	16.4	26.0	0.5	87.6	49.9	64.2	6.5	74.7	34.7	69.7	36.8	58.0	19.6	32.3	50	50.85	37.1
DenseASPP [52]	78.1	20.5	18.2	20.0	16.6	27.8	28.9	5.7	88.5	53.3	67.5	9.3	76.3	39.6	70.0	36.8	57.7	15.9	32.4	20	23.43	40.2
SqueezeSeg [12]	68.8	16.0	4.1	3.3	3.6	12.9	13.1	0.9	85.4	26.9	54.3	4.5	57.4	29.0	60.0	24.3	53.7	17.5	24.5	66	1	29.5
SqueezeSeg + CRF [12]	68.3	18.1	5.1	4.1	4.8	16.5	17.3	1.2	84.9	28.4	54.7	4.6	61.5	29.2	59.6	25.5	54.7	11.2	36.3	55	1	30.8
SqueezeSegV2 [13]	81.8	18.5	17.9	13.4	14.0	20.1	25.1	3.9	88.6	45.8	67.6	17.7	73.7	41.1	71.8	35.8	60.2	20.2	36.3	50	1	39.7
SqueezeSegV2 + CRF [13]	82.7	21.0	22.6	14.5	15.9	20.2	24.3	2.9	88.5	42.4	65.5	18.7	73.8	41.0	68.5	36.9	58.9	12.9	41.0	40	1	39.6
RangeNet21 [14]	85.4	26.2	26.5	18.6	15.6	31.8	33.6	4.0	91.4	57.0	74.0	26.4	81.9	52.3	77.6	48.4	63.6	36.0	50.0	20	25	47.4
RangeNet53 [14]	86.4	24.5	32.7	25.5	22.6	36.2	33.6	4.7	91.8	64.8	74.6	27.9	84.1	55.0	78.3	50.1	64.0	38.9	52.2	13	50.4	49.9
RangeNet53 + kNN [14]	91.4	25.7	34.4	25.7	23.0	38.3	38.8	4.8	91.8	65.0	75.2	27.8	87.4	58.6	80.5	55.1	64.6	47.9	55.9	12	50.4	52.2
MINet	85.2	38.2	32.1	29.3	23.1	47.6	46.8	24.5	90.5	58.8	72.1	25.9	82.2	49.5	78.8	52.5	65.4	37.7	55.5	59	1	52.4
MINet + kNN	90.1	41.8	34.0	29.9	23.6	51.4	52.4	25.0	90.5	59.0	72.6	25.8	85.6	52.3	81.1	58.1	66.1	49.0	59.9	47	1	55.2

TABLE 6: Evaluation results on the SemanticKITTI test split for point-based, image-based, and projection-based methods. The proposed Multi-scale Interaction Network (MINet) performs well for small objects.

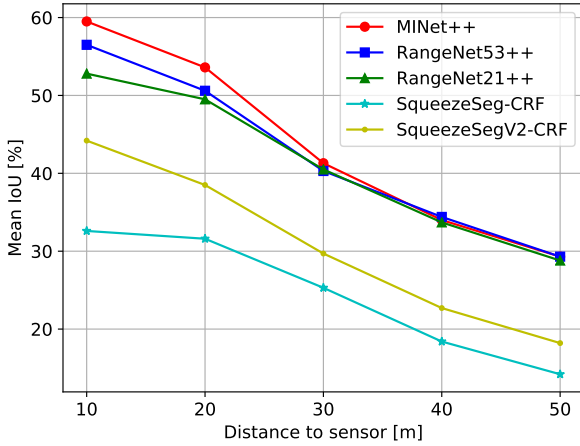


Fig. 5: Accuracy of different projection-based methods based on the distance to the sensor. ++ denotes k NN post-processing.

As for image-based methods, we use four widely used methods, namely PSPNet [2], DeepLabV3+ [22], DenseASPP [52], which has been designed for the autonomous driving scenario, and the lightweight model BiSeNet [51]. We adjust the input channels so that these methods can be applied to the projected image. While these methods are faster than point-based methods, they have by far more parameters and the accuracy is significantly lower. This shows that projected LiDAR data cannot be directly processed by image-based segmentation methods since the modality differs from RGB images.

We also compare our approach to other projection-based methods. While SqueezeSeg [12], [13] has the same amount of parameters and depending on the setting runs slightly faster, the accuracy is very low. The state-of-the-art projection-based method RangeNet [14] outperforms SqueezeSeg in terms of accuracy, but this is achieved by increasing the number of parameters to over 50M and decreasing the runtime. Our approach is much more efficient. It uses only 2% of the number of parameters compared to RangeNet53 and it is about 4× faster while achieving a higher accuracy. Fig. 4 visualizes the accuracy and runtime of the methods of Tab. 6 and shows the effectiveness and

efficiency of the proposed approach.

Fig. 5 analyzes where our method gains in accuracy compared to other projection-based methods, in particular RangeNet [14]. The main improvement is achieved for points that are within a radius of 30 meters. This is expected since the bottom branch, which has the lowest resolution and therefore focuses on close objects, uses the most expensive operations. For objects that are far away, heavy networks like RangeNet, however, also do not perform better. Some qualitative results from the SemanticKITTI validation set are shown in Fig. 6 and Fig. 7.

We also evaluate our method on SemanticPOSS [45] and compare our approach to other projection-based methods in Tab. 7. Since the dataset is smaller and the point clouds are more sparse compared to SemanticKITTI, the mIoU is lower for all methods. However, our approach handles the small size and sparseness much better than RangeNet and the mIoU is by more than 12% higher. This is partially due to the high number of parameters, which make RangeNet prone to overfitting. In contrast to k NN, the CRF decreases the accuracy for SqueezeSeg due to the sparseness of the points.

4.4 Performance on an Embedded Platform

We finally compare our method with RangeNet on an embedded platform. We use a Jetson AGX, which is an AI module for embedded systems as they are used for autonomous driving, and optimize all methods by TensorRT. The results are shown in Tab. 8 and visualized in Fig. 8. Since the input resolution can be decreased to reduce the runtime, we report the results for three different input resolutions. We can see that at each resolution, the Multi-scale Interaction Network outperforms RangeNet53 with or without post-processing. Furthermore, it is much faster than RangeNet53. Even with full resolution and post-processing, the Multi-scale Interaction Network runs in real-time since the LiDAR scan frequency is 10Hz. Compared to Tab. 6 where the runtime is measured on a workstation with a single Quadro P6000, the post-processing has a higher impact on the runtime for the embedded platform since it is not optimized. Furthermore, the post-processing is performed on the point cloud and it does not benefit from reducing the resolution of the projected image. The Multi-scale Interaction Network

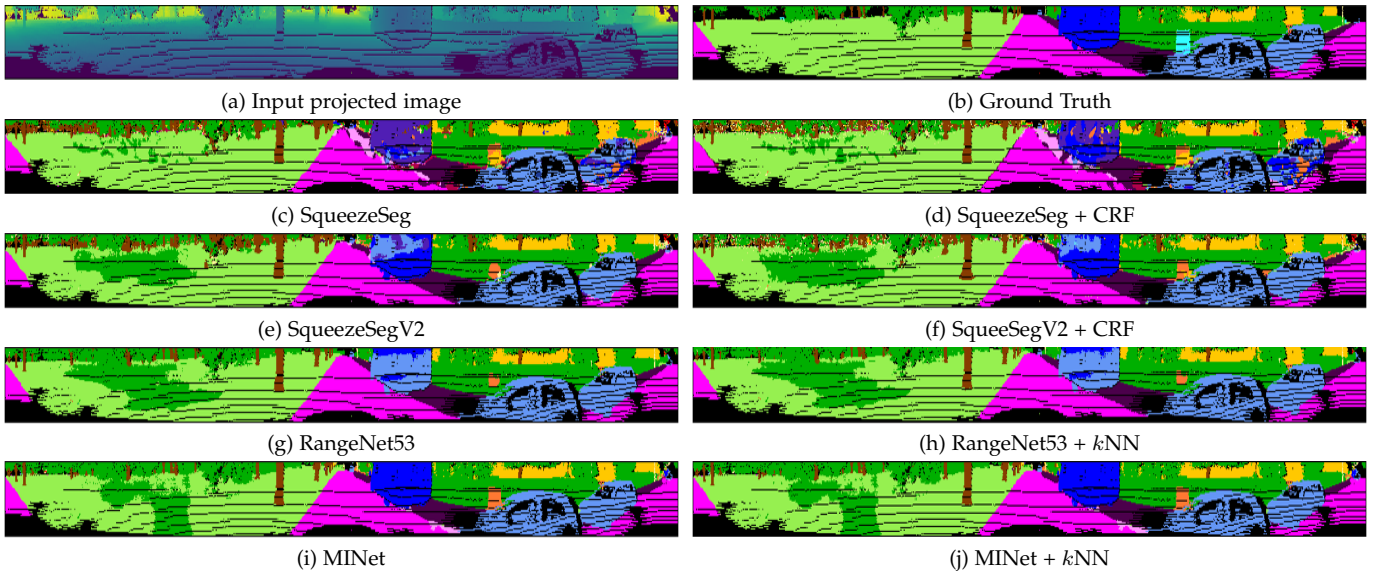


Fig. 6: Qualitative results. For the input image, we only show the range.

	person	rider	car	truck	plants	traffic sign	pole	trashcan	building	cone/stone	fence	bike	ground	mIoU
SqueezeSeg [12]	14.2	1.0	13.2	10.4	28.0	5.1	5.7	2.3	43.6	0.2	15.6	31.0	75.0	18.9
SqueezeSeg + CRF [12]	6.8	0.6	6.7	4.0	2.5	9.1	1.3	0.4	37.1	0.2	8.4	18.5	72.1	12.9
SqueezeSegV2 [13]	48.0	9.4	48.5	11.3	50.1	6.7	6.2	14.8	60.4	5.2	22.1	36.1	71.3	30.0
SqueezeSegV2 + CRF [13]	43.9	7.1	47.9	18.4	40.9	4.8	2.8	7.4	57.5	0.6	12.0	35.3	71.3	26.9
RangeNet53 [14]	55.7	4.5	34.4	13.7	57.5	3.7	6.6	23.3	64.9	6.1	22.2	28.3	72.9	30.3
RangeNet53 + kNN [14]	57.3	4.6	35.0	14.1	58.3	3.9	6.9	24.1	66.1	6.6	23.4	28.6	73.5	30.9
MINet	61.8	12.0	63.3	22.2	68.1	16.3	29.3	28.5	74.6	25.9	31.7	44.5	76.4	42.7
MINet + kNN	62.4	12.1	63.8	22.3	68.6	16.7	30.1	28.9	75.1	28.6	32.2	44.9	76.3	43.2

TABLE 7: Evaluation results on the SemanticPOSS validation split. The proposed Multi-scale Interaction Network (MINet) achieves the best accuracy for all classes.

Approach	Resolution	GFLOPs	SPS	mIoU
RangeNet53 [14]	64 × 2048	360.5	7	49.9
	64 × 1024	180.3	11	45.4
	64 × 512	90.1	22	39.3
RangeNet53++ [14]	64 × 2048	360.5	5	52.2
	64 × 1024	180.3	8	48.0
	64 × 512	90.1	13	41.9
MINet	64 × 2048	6.2	24	52.4
	64 × 1024	3.2	47	49.1
	64 × 512	1.7	80	45.0
MINet++	64 × 2048	6.2	13	55.2
	64 × 1024	3.2	18	52.4
	64 × 512	1.7	21	48.5

TABLE 8: Performance on an embedded platform (Jetson AGX). The number of GFLOPs does not include the post-processing.

is about 4× faster than RangeNet53 without post-processing and 2× faster with post-processing.

5 CONCLUSION

In this work, we proposed a novel lightweight projection-based method, called Multi-scale Interaction Network (MINet), for semantic segmentation of LiDAR data. The network is highly efficient and runs in real-time on GPUs and embedded platforms. It outperforms point-based, image-based, and projection-based methods in terms of accuracy, number of parameters, and runtime. This has been

achieved by using a multi-scale approach where the computational resources are balanced between the scales and by introducing interactions between the scales. By processing the modalities separately before fusing them and adding additional different types of supervision, we could further improve the accuracy without decreasing the runtime. Compared to the state-of-the-art projection-based method RangeNet, the Multi-scale Interaction Network reduces the number of parameters by 98% and it is 4× faster while achieving a higher accuracy. Since the Multi-scale Interaction Network processes more than 24 scans per second on an embedded platform, it can be used for autonomous driving.

ACKNOWLEDGMENTS

The authors would like to thank...

REFERENCES

- [1] J. Long, E. Shelhamer, and T. Darrell, "Fully convolutional networks for semantic segmentation," in *IEEE CVPR*, 2015, pp. 3431–3440.
- [2] H. Zhao, J. Shi, X. Qi, X. Wang, and J. Jia, "Pyramid scene parsing network," in *IEEE CVPR*, 2017, pp. 2881–2890.
- [3] Z. Huang, X. Wang, L. Huang, C. Huang, Y. Wei, and W. Liu, "CCNet: Criss-cross attention for semantic segmentation," in *IEEE ICCV*, 2019, pp. 603–612.
- [4] Z. Zhu, M. Xu, S. Bai, T. Huang, and X. Bai, "Asymmetric non-local neural networks for semantic segmentation," in *IEEE ICCV*, 2019, pp. 593–602.

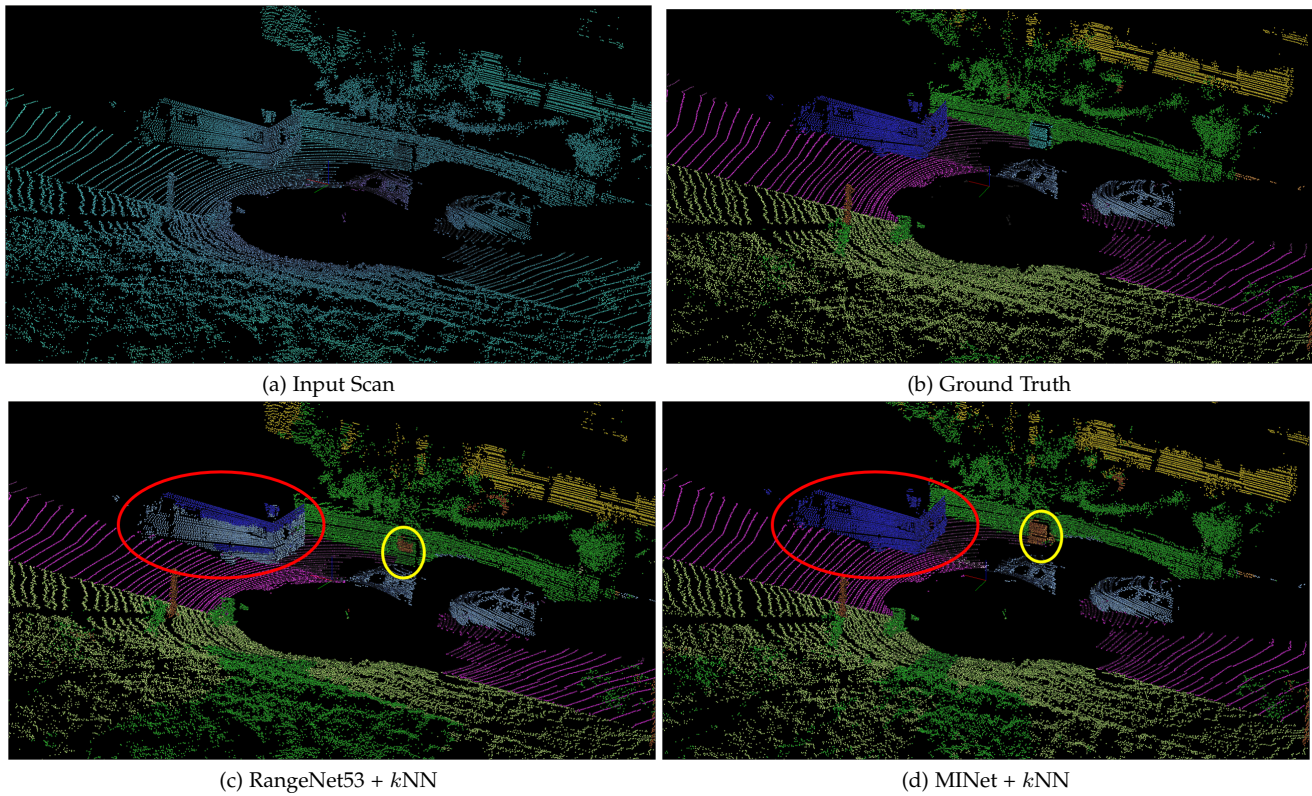


Fig. 7: Qualitative results. RangeNet segments most points of the truck as a car, while MINet segments the truck correctly (red circle). In some cases, both approaches fail (yellow circle). Although MINet segments the object correctly, it misclassifies it.

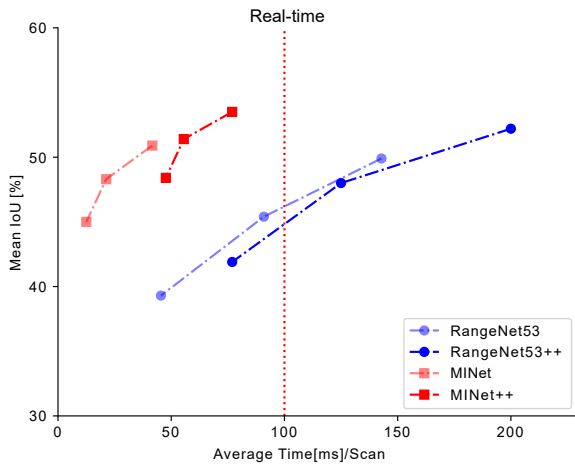


Fig. 8: Visualization of Tab. 8. For each method, the three points on its curve correspond to the three different input resolutions 64×512 , 64×1024 , and 64×2048 from left to right. The Multi-scale Interaction Network runs in real-time on a Jetson AGX with full resolution and post-processing.

[5] X. Zhang, Y. Wei, Y. Yang, and T. S. Huang, "Sg-one: Similarity guidance network for one-shot semantic segmentation," *IEEE Transactions on Cybernetics*, 2020.

[6] D. Lin, R. Zhang, Y. Ji, P. Li, and H. Huang, "Scn: Switchable context network for semantic segmentation of rgb-d images," *IEEE transactions on Cybernetics*, 2018.

[7] S. Chen, B. Wang, X. Tan, and X. Hu, "Embedding attention and residual network for accurate salient object detection," *IEEE transactions on Cybernetics*, 2018.

[8] C. R. Qi, H. Su, K. Mo, and L. J. Guibas, "PointNet: Deep learning

on point sets for 3D classification and segmentation," in *IEEE CVPR*, 2017, pp. 652–660.

[9] C. R. Qi, L. Yi, H. Su, and L. J. Guibas, "PointNet++: Deep hierarchical feature learning on point sets in a metric space," in *NIPS*, 2017, pp. 5099–5108.

[10] Y. Li, R. Bu, M. Sun, W. Wu, X. Di, and B. Chen, "PointCNN: Convolution on \mathcal{X} -transformed points," in *NIPS*, 2018, pp. 820–830.

[11] W. Wu, Z. Qi, and L. Fuxin, "PointConv: Deep convolutional networks on 3D point clouds," in *IEEE CVPR*, 2019, pp. 9621–9630.

[12] B. Wu, A. Wan, X. Yue, and K. Keutzer, "SqueezeSeg: Convolutional neural nets with recurrent CRF for real-time road-object segmentation from 3D LiDAR point cloud," in *IEEE ICRA*. IEEE, 2018, pp. 1887–1893.

[13] B. Wu, X. Zhou, S. Zhao, X. Yue, and K. Keutzer, "SqueezeSegV2: Improved model structure and unsupervised domain adaptation for road-object segmentation from a LiDAR point cloud," in *IEEE ICRA*. IEEE, 2019, pp. 4376–4382.

[14] A. Milioto, I. Vizzo, J. Behley, and C. Stachniss, "RangeNet++: Fast and accurate LiDAR semantic segmentation," in *IEEE/RSJ IROS*, 2019.

[15] H. Zhang, K. Dana, J. Shi, Z. Zhang, X. Wang, A. Tyagi, and A. Agrawal, "Context encoding for semantic segmentation," in *IEEE CVPR*, 2018, pp. 7151–7160.

[16] Y. Liu, M.-M. Cheng, X. Hu, J.-W. Bian, L. Zhang, X. Bai, and J. Tang, "Richer convolutional features for edge detection," *IEEE TPAMI*, vol. 41, no. 8, pp. 1939–1946, 2019.

[17] Y. Liu, M.-M. Cheng, D.-P. Fan, L. Zhang, J. Bian, and D. Tao, "Semantic edge detection with diverse deep supervision," *arXiv preprint arXiv:1804.02864*, 2018.

[18] O. Ronneberger, P. Fischer, and T. Brox, "U-Net: Convolutional networks for biomedical image segmentation," in *MICCAI*. Springer, 2015, pp. 234–241.

[19] L.-C. Chen, G. Papandreou, I. Kokkinos, K. Murphy, and A. L. Yuille, "Semantic image segmentation with deep convolutional nets and fully connected CRFs," *arXiv preprint arXiv:1412.7062*, 2014.

- [20] —, “DeepLab: Semantic image segmentation with deep convolutional nets, atrous convolution, and fully connected crfs,” *IEEE TPAMI*, vol. 40, no. 4, pp. 834–848, 2017.
- [21] L.-C. Chen, G. Papandreou, F. Schroff, and H. Adam, “Rethinking atrous convolution for semantic image segmentation,” *arXiv preprint arXiv:1706.05587*, 2017.
- [22] L.-C. Chen, Y. Zhu, G. Papandreou, F. Schroff, and H. Adam, “Encoder-decoder with atrous separable convolution for semantic image segmentation,” in *ECCV*, 2018, pp. 801–818.
- [23] J. Fu, J. Liu, H. Tian, Y. Li, Y. Bao, Z. Fang, and H. Lu, “Dual attention network for scene segmentation,” in *IEEE CVPR*, 2019, pp. 3146–3154.
- [24] X. Wang, R. Girshick, A. Gupta, and K. He, “Non-local neural networks,” in *IEEE CVPR*, 2018, pp. 7794–7803.
- [25] A. G. Howard, M. Zhu, B. Chen, D. Kalenichenko, W. Wang, T. Weyand, M. Andreetto, and H. Adam, “Mobilenets: Efficient convolutional neural networks for mobile vision applications,” *arXiv preprint arXiv:1704.04861*, 2017.
- [26] M. Sandler, A. Howard, M. Zhu, A. Zhmoginov, and L.-C. Chen, “Mobilenetv2: Inverted residuals and linear bottlenecks,” in *IEEE CVPR*, 2018, pp. 4510–4520.
- [27] A. Howard, M. Sandler, G. Chu, L.-C. Chen, B. Chen, M. Tan, W. Wang, Y. Zhu, R. Pang, V. Vasudevan *et al.*, “Searching for mobilenetv3,” in *IEEE CVPR*, 2019, pp. 1314–1324.
- [28] X. Zhang, X. Zhou, M. Lin, and J. Sun, “Shufflenet: An extremely efficient convolutional neural network for mobile devices,” in *IEEE CVPR*, 2018, pp. 6848–6856.
- [29] N. Ma, X. Zhang, H.-T. Zheng, and J. Sun, “Shufflenet v2: Practical guidelines for efficient cnn architecture design,” in *ECCV*, 2018, pp. 116–131.
- [30] M. Tatarchenko, J. Park, V. Koltun, and Q.-Y. Zhou, “Tangent convolutions for dense prediction in 3D,” in *IEEE CVPR*, 2018, pp. 3887–3896.
- [31] H. Thomas, C. R. Qi, J.-E. Deschaud, B. Marcotegui, F. Goulette, and L. J. Guibas, “KPConv: Flexible and deformable convolution for point clouds,” in *IEEE ICCV*, 2019, pp. 6411–6420.
- [32] L. Landrieu and M. Simonovsky, “Large-scale point cloud semantic segmentation with superpoint graphs,” in *IEEE CVPR*, 2018, pp. 4558–4567.
- [33] Q. Hu, B. Yang, L. Xie, S. Rosa, Y. Guo, Z. Wang, N. Trigoni, and A. Markham, “Randla-net: Efficient semantic segmentation of large-scale point clouds,” *arXiv preprint arXiv:1911.11236*, 2019.
- [34] S. Li, Y. Liu, and J. Gall, “Projected-point-based segmentation: A new paradigm for lidar point cloud segmentation,” *arXiv preprint arXiv:2008.03928*, 2020.
- [35] F. N. Iandola, S. Han, M. W. Moskewicz, K. Ashraf, W. J. Dally, and K. Keutzer, “SqueezeNet: AlexNet-level accuracy with 50x fewer parameters and 10.5MB model size,” *arXiv preprint arXiv:1602.07360*, 2016.
- [36] J. Redmon and A. Farhadi, “YOLOv3: An incremental improvement,” *arXiv preprint arXiv:1804.02767*, 2018.
- [37] X. Chen, A. Milioto, E. Palazzolo, P. Giguère, J. Behley, and C. Stachniss, “SuMa++: Efficient LiDAR-based Semantic SLAM,” in *IEEE/RSJ IROS*, 2019.
- [38] X. Chen, T. Labe, A. Milioto, T. Röhling, O. Vysotska, A. Haag, J. Behley, and C. Stachniss, “OverlapNet: Loop Closing for LiDAR-based SLAM,” in *RSS*, 2020.
- [39] K. He, X. Zhang, S. Ren, and J. Sun, “Deep residual learning for image recognition,” in *IEEE CVPR*, 2016, pp. 770–778.
- [40] C.-Y. Lee, S. Xie, P. Gallagher, Z. Zhang, and Z. Tu, “Deeply-supervised nets,” in *Artificial Intelligence and Statistics*, 2015, pp. 562–570.
- [41] C. Yu, J. Wang, C. Peng, C. Gao, G. Yu, and N. Sang, “Learning a discriminative feature network for semantic segmentation,” in *IEEE CVPR*, 2018, pp. 1857–1866.
- [42] A. Kirillov, E. Levinkov, B. Andres, B. Savchynskyy, and C. Rother, “InstanceCut: from edges to instances with MultiCut,” in *IEEE CVPR*, 2017, pp. 5008–5017.
- [43] M. Berman, A. Rannen Triki, and M. B. Blaschko, “The Lovász-softmax loss: A tractable surrogate for the optimization of the intersection-over-union measure in neural networks,” in *IEEE CVPR*, 2018, pp. 4413–4421.
- [44] J. Behley, M. Garbade, A. Milioto, J. Quenzel, S. Behnke, C. Stachniss, and J. Gall, “SemanticKITTI: A dataset for semantic scene understanding of LiDAR sequences,” in *IEEE ICCV*, 2019, pp. 9297–9307.
- [45] Y. Pan, B. Gao, J. Mei, S. Geng, C. Li, and H. Zhao, “Semanticpos: A point cloud dataset with large quantity of dynamic instances,” *arXiv preprint arXiv:2002.09147*, 2020.
- [46] A. Geiger, P. Lenz, and R. Urtasun, “Are we ready for autonomous driving? The KITTI vision benchmark suite,” in *IEEE CVPR*, 2012, pp. 3354–3361.
- [47] M. Everingham, S. A. Eslami, L. Van Gool, C. K. Williams, J. Winn, and A. Zisserman, “The pascal visual object classes challenge: A retrospective,” *IJCV*, vol. 111, no. 1, pp. 98–136, 2015.
- [48] H. Su, V. Jampani, D. Sun, S. Maji, E. Kalogerakis, M.-H. Yang, and J. Kautz, “SPLATNet: Sparse lattice networks for point cloud processing,” in *IEEE CVPR*, 2018, pp. 2530–2539.
- [49] Y. Zhang, Z. Zhou, P. David, X. Yue, Z. Xi, B. Gong, and H. Foroosh, “Polarnet: An improved grid representation for online lidar point clouds semantic segmentation,” in *IEEE CVPR*, 2020, pp. 9601–9610.
- [50] H. Li, P. Xiong, J. An, and L. Wang, “Pyramid attention network for semantic segmentation,” *arXiv preprint arXiv:1805.10180*, 2018.
- [51] C. Yu, J. Wang, C. Peng, C. Gao, G. Yu, and N. Sang, “Bisenet: Bilateral segmentation network for real-time semantic segmentation,” in *ECCV*, 2018, pp. 325–341.
- [52] M. Yang, K. Yu, C. Zhang, Z. Li, and K. Yang, “Denseaspp for semantic segmentation in street scenes,” in *IEEE CVPR*, 2018, pp. 3684–3692.



Shijie Li received his bachelor's degree in Automation Engineering from University of Electronic Science and Technology of China in 2016 and his master's degree in computer science from the Nankai University in 2019. Since 2019, he is a Ph.D. student at the University of Bonn. His research interests include action recognition and scene understanding.



Xieyuanli Chen is a Ph.D. student at the Photogrammetry and Robotics lab, University of Bonn, and also a member of the Technical Committee of RoboCup Rescue Robot League. He received his master's degree in Robotics in 2017 at the National University of Defense Technology, China, and his bachelor's degree in Electrical Engineering and Automation in 2015 at Hunan University, China.



Yun Liu is a Ph.D. candidate at College of Computer Science, Nankai University. He received his bachelor's degree from Nankai University in 2016. His research interests include computer vision and machine learning.



Dengxin Dai is a lecturer working with the Computer Vision Lab at ETH Zurich. He is leading the research group TRACE-Zurich working on Autonomous Driving within the R&D project “TRACE: Toyota Research on Automated Cars in Europe”. In 2016, he obtained his Ph.D. at ETH Zurich under the supervision of Prof. Luc Van Gool and Prof. Gerhard Schmitt. During the Ph.D. study, he was working on the project VarCity for City Modeling based on camera data.



Cyrill Stachniss is a full professor at the University of Bonn and heads the Photogrammetry and Robotics Lab. Before working in Bonn, he was a lecturer at the University of Freiburg in Germany and a senior researcher at the Swiss Federal Institute of Technology. Cyrill Stachniss finished his habilitation in 2009 and received his Ph.D. thesis entitled Exploration and Mapping with Mobile Robots at the University of Freiburg in 2006.



Juergen Gall obtained his bachelor's and his master's degree in mathematics from the University of Wales Swansea (2004) and from the University of Mannheim (2005). In 2009, he obtained a Ph.D. in computer science from the Saarland University and the Max Planck Institut fr Informatik. He was a postdoctoral researcher at the Computer Vision Laboratory, ETH Zurich, from 2009 until 2012 and senior research scientist at the Max Planck Institute for Intelligent Systems in Tbingen from 2012 until 2013. Since 2013, he is a professor at the University of Bonn and head of the Computer Vision Group.